



TECHNICAL ARTICLE

Evaluating the Microstructural, Mechanical, and Electrochemical Behavior of Spark Plasma-Assisted Dissimilar Joining of 17-4 PH Stainless Steel to Inconel 718

D. Praveen Kumar and S. Kumaran

Submitted: 26 September 2022 / Revised: 3 November 2022 / Accepted: 19 November 2022 / Published online: 5 December 2022

In this study, the spark plasma sintering (SPS) technique was used to join 17-4 martensitic precipitation-hardened stainless steel (17-4PH SS) with Inconel 718, a nickel-based superalloy (IN 718). Spark plasma-assisted diffusion bonding was done at a temperature of 850 °C with a bonding time of 5 min under the pressure of 50 MPa. Ansys simulation was used to examine the temperature distribution and displacement during joule heating, and it was then compared to the experimental data that had been gathered. With the help of a field emission scanning electron microscope, a white conduit at the bonded zone is evident for the diffusion of elements. Electron backscatter diffraction analysis reveals the random and elongated grains, free from local residual plastic strain at the diffusion zone. Electron probe micro-analysis was used to point out the elemental diffusion among dissimilar alloys. It is observed that the elements from IN 718 are diffused to 17-4 PH SS. At the diffusion zone, there is an increment in hardness of 345 ± 10 Hv due to the diffusion of Ni and other elements. The SPS diffusion-bonded samples have an ultimate strength of 708 ± 5 MPa with an elongation of $9 \pm 2\%$. Dissolution of precipitates and $M_{23}C_6$ during diffusion bonding and segregation of Nb; Ti-rich carbide deteriorate the hardness and tensile properties of the bond zone which leads to a strain-free brittle fracture. An electrochemical polarization and impedance study was done in a 3.5% NaCl solution. After SPS diffusion bonding, 17-4 PH has lower corrosion resistance when compared to other regions.

Keywords diffusion bonding, dissimilar joining, spark plasma sintering, 17-4PH SS/IN 718

1. Introduction

The Inconel 718 alloy has excellent mechanical properties at elevated temperatures of up to 700 °C due to its gamma prime (γ') strengthening (Ref 1), as well as cryogenic temperature. There are many applications for Inconel 718, such as gas turbine components, jet engines, cryogenic storage tanks, pump bodies, thrust reversers, rocket motors, nuclear fuel element spacers, and hot extrusion tooling (Ref 2). The 17-4 PH grade of stainless steel is martensitic stainless steel which is hardened by precipitation. In both base metals and welds, 17-4 stainless steel has high strength, good corrosion resistance, and toughness. The corrosion resistance of this material is comparable to that of grade 304. The stainless steel alloy is used in a wide range of industries, including chemical, paper, and food processing, and it resists corrosion better than most hardenable

stainless steels. With these properties, designers can simplify fabrication and often reduce their costs while enhancing product reliability. 316 °C is the maximum temperature at which high strength is maintained. The 17-4PH alloy resists stress corrosion cracking well at higher aging temperatures. Joining these two dissimilar materials is applicable in aerospace industries, especially when comes to the combustion chamber in gas turbine assembly. Turbine blades are made of 17-4PH SS and joined with the rotor shaft using Inconel 718. While joining the 17-4 PH SS and IN 718 alloys by the fusion welding process, there is a formation of laves phases in IN718 and segregation of NbC in IN 718 (Ref 3-11). These laves phases and agglomeration of particles have led to brittle failure at the welded zone. Researchers had previously investigated 17-4 PH SS diffusion bonding with IN718 using conventional bonding methods (Ref 12). However, the extended processing time, longer holding time, higher pressure, and slower heating rate were notable drawbacks. Significant consequences resulted, including premature failure, segregation, notorious phase formations, microstructural defects, bulging, and localized stress generation.

Spark plasma sintering (SPS) is a versatile solid-state joining technique like micro-arc welding, electric resistance welding, and diffusion welding (Ref 13). Similar/dissimilar engineered alloys are bonded in a short span of time using DC pulse current which passes throughout the workpieces (Ref 14-17). Modern studies have demonstrated the possibility of spark plasma-assisted diffusion bonding for the development of novel

D. Praveen Kumar and S. Kumaran, Department of Metallurgical and Materials Engineering, National Institute of Technology, Tiruchirappalli, Tamil Nadu 620015, India. Contact e-mails: praveen.annauniv@gmail.com and kumara@nitt.edu.

Table 1 Chemical compositions of the as-received 17-4 PH stainless steel

Material	Cr	Ni	Cu	Mn	C	Si	Mo	Nb	Fe
17-4 PH SS	15.85	4.7	3.31	0.96	0.034	0.36	0.28	0.28	Bal

materials joining and functionally graded material systems. In the domain of joining dissimilar materials, SPS technology has emerged as one of the most significant and influential approaches. Compared with conventional methods, spark plasma-assisted diffusion bonding can overcome these practical challenges by localized *in situ* Joule heating and rapid processing. Ansys is a FEA computer program; using this numerical software analysis, thermal behavior and stress distribution can be simulated in the 3D module. In this study, Ansys simulations are used to predict the SPS parameters (temperature distribution and total deformation) inside the graphite die (Ref 18-20). In IN718 passive protection, layers are made of the double-layer structure. The loose outer layer associated with the high-frequency time constant and hydroxides of iron and nickel have n-type characteristics (Ref 21). The dense inner layer related to the low-frequency time constant is rich in chromium oxides. In 17-4PH SS apart from passive layer formation, other factors like austenite-to-martensite transformation ratio, size of lath martensite, morphology, and density of carbides lead to corrosion resistance.

While several studies have been conducted on the diffusion bonding between nickel alloys and stainless steels, the experimental prospectus has not yet elucidated the effect of SPS pulse currents on diffusion kinetics between IN 718 and 17-4PH SS. Obtaining excellent mechanical properties and superior bonding characteristics is essential for which it is required to understand the process parameters and process kinetics. This study examines the effect of pulse current on the structural evolution, mechanical properties, and electrochemical attributes of IN 718 to 17-4 PH SS during spark plasma-assisted diffusion bonding.

2. Materials and Methods

The chemical compositions of 17-4 PH stainless steel and IN 718 superalloy are given in Tables 1 and 2. The alloys for diffusion bonding were cut into the dimension of 20 mm in diameter and 10 mm in height. The alloys were mirror-polished using emery sheets followed by alumina polishing for maintaining the surface roughness at 0.07 and 0.08. The surface roughness of the alloy was measured using mitutoyo surftrsr SJ-210. Alumina present in the polished alloy was removed using ultrasonic bath containing acetone. The bonding of dissimilar alloys was carried out by a spark plasma heating method (Model: SPS-515S DR.SINTER LAB, SPS SYNTEX INC, Japan). The alloys were placed into the graphite die and loaded into the SPS chamber. The vacuum atmosphere was maintained as 10^{-2} torr inside the chamber. The heating rate was maintained at 50 °C/min, and bonding was done at the temperature of 850 °C for 5 min dwell period having a uniaxial load of 50 MPa.

Table 2 Chemical compositions of the as-received Inconel 718 alloy

Material	Cr	Fe	Nb	Mo	Ti	Al	Mn	Si	C	Ni
Inconel-718	18.2	19.5	5.2	2.8	1	0.6	0.1	0.1	0.05	Bal

The schematic line diagram of the SPS machine with the bonded samples is described in Fig. 1. The graphite die with 17-4 PH SS/IN 718 alloy samples' half-sectional views has been modeled for a better understanding of the temperature distribution and total deformation. Aqua regia and Kalling No: 2 were used as the etchant. Optical microscopy was used to analyze the microstructure of bonded samples (Olympus BX53) and field emission scanning electron microscope (CARL ZEISS, SUPRA 55VP). Electron backscatter diffraction (EBSD) with CMOS detector was used to analyze the diffusion zone grain formation and understand the elemental distribution. An electron probe micro-analyzer (Jeol JXA-2830) was used to analyze the elemental concentration at the diffusion zone.

A Vickers hardness tester (Wilson hardness machine 402 MVD) was used to measure the hardness according to ASTM E92-16 standards. Indentation was made at a load of 10 g at a distance of every 15 μ m repeating 3 cycles for attaining average results. The flat dog-bone-shaped tensile samples maintaining ASTM E8-04 standards, and specimens with 6 mm gauge length and 1 mm thickness were extracted from the center of bonded samples using wire cut electrical discharge machining. The mean tensile values were evaluated by testing four samples in each condition having a strain rate of 10^{-3} s⁻¹ with the help of universal testing machine (Dak system inc, model: T-72302). The electrochemical linear polarization and Nyquist plots were intended (Biological Instruments SP 150) using 3.5% NaCl solution following ASTM G102-89.

3. Results and Discussion

3.1 Ansys Simulation and Experimental Data

The SPS data derived during diffusion bonding of dissimilar alloy are shown in Fig. 2. Time vs. temperature/current/displacement curves are presented in Fig. 2(a). When bonding at 850 °C for 5 min at a heating rate of 50 °C/min, the peak current of 870 A is reached for the set temperature of 850 °C, and the average current consumed during bonding for 5 min is 763 A at given temperature. Under uniaxial pressure (50 MPa), samples expand by 0.8 mm and contract by -1.5 mm on the z-axis. The displacement signal includes not only the sample shrinkage but also the volumetric change of the graphite die due to applied pressure and the temperature change. Figure 2(b) shows the 3D module used for simulation with contact resistance as R1 to R5 when the current flows from the cathode to the anode through the samples. Contact resistance is the highest resistance of all, so the heat is generated at the faying surface. Figure 2(c) shows a simulated temperature distribution from Ansys. During diffusion bonding, the surface temperature is higher on the faying surface than on the sample surfaces. From the simulated temperature distribution, R1 and R5 have a

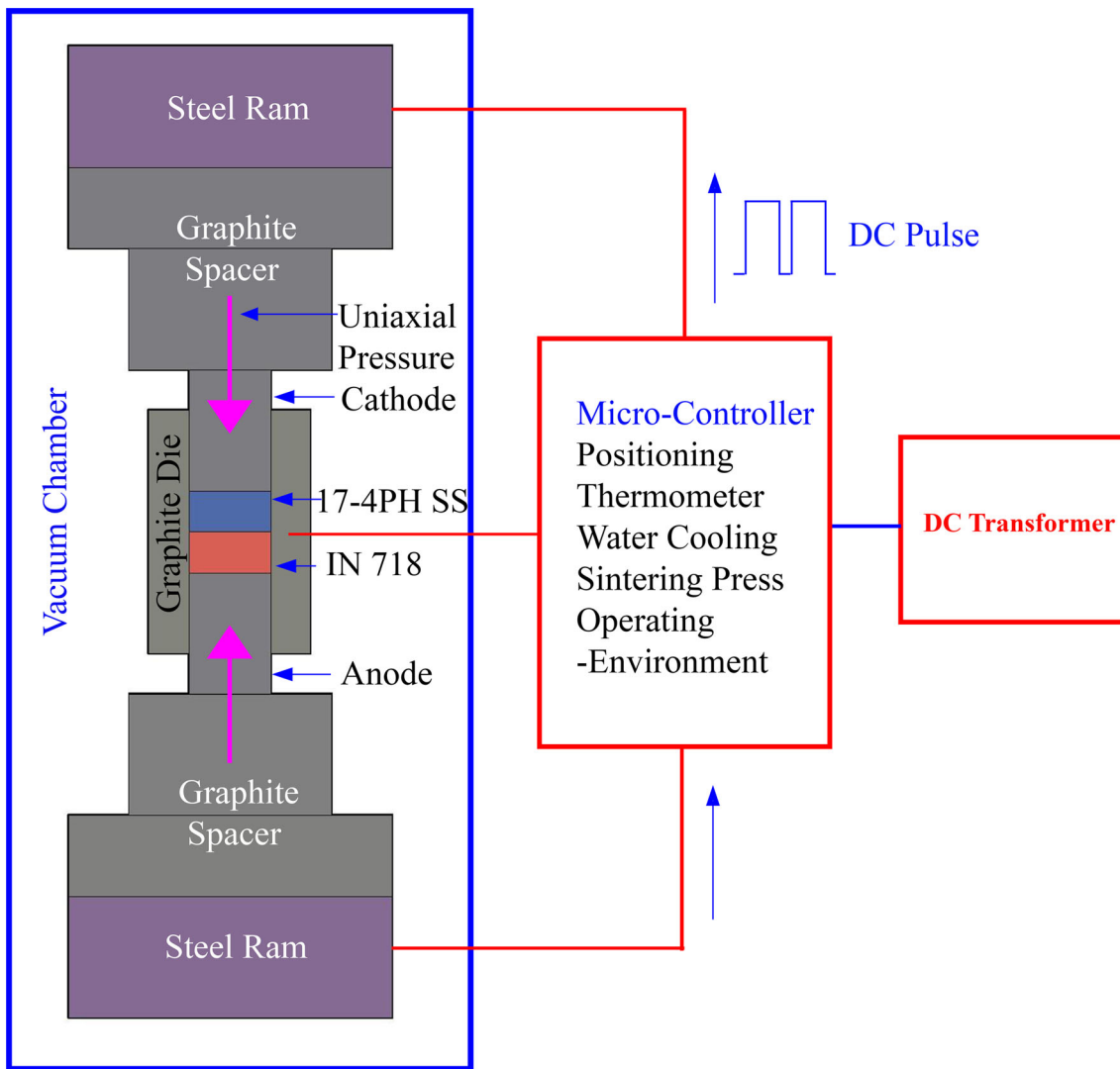


Fig. 1 Schematic line diagram of SPS machine with the graphite die, plungers, and samples

higher temperature range of up to 1480 °C, and the contact resistance between graphite plungers and the samples (R2 and R4) leads to a range of 1130 °C. The diffusion zone has a temperature range of 1300 °C, because of the contact resistance between Inconel 718 and 17-4 PHSS (R3). This helps the diffusion bonding process to be completed faster. The maximum deformation (0.53 mm) is obtained on the Inconel 718 sample as shown in Fig. 2(d). At high temperature and pressure, FCC (IN 718) slip planes are easily activated when compared to BCT (17-4PH SS). Using Ansys simulation based on processing data, the spark plasma heating technique is found to be effective for diffusion bonding.

3.2 Microstructure of as-Received and Diffusion-Bonded Dissimilar Alloy

Figure 3(a) shows the optical micrograph of as-received 17-4 PH stainless steel having a martensitic matrix with strings of δ -ferrite and prior austenitic grains with an average grain size of $22 \pm 1 \mu\text{m}$. Figure 3(b) shows the micrographs of as-received Inconel 718 alloy exhibiting fine equiaxed grains having a grain size of $9 \pm 1 \mu\text{m}$ with annealing twins. Figure 3(c) and (d)

shows the 17-4 PH SS and Inconel 718 after diffusion bonding at 850 °C for 5 min. The chosen temperature is the solutionizing temperature of the alloys. So it is believed that both alloys have been solutionized at a given temperature. After diffusion bonding, both the materials have gone through some grain size modification. In 17-4 PH stainless steel, there is some grain refinement of $8 \pm 1 \mu\text{m}$, and in IN 718, there is a grain coarsening of $20 \pm 2 \mu\text{m}$. Figure 3(e) shows the SEM images of diffusion-bonded dissimilar alloy. There are no voids visible in the bond zone. The etched sample has a white conduit of less than $3 \mu\text{m}$ which is evident that the materials are diffused.

3.3 Electron Backscatter Diffraction (EBSD) and Electron Probe Micro-analysis

Figure 4(a) shows the Image Quality Map (IQM), of spark plasma-assisted diffusion bonding of dissimilar alloys. It exhibits a void-free diffusion zone with the recrystallized grains. Figure 4(b) shows the phase map having a body-centered cubic structure of 17-4PH and face-centered in IN 718 without any segregation in the parent and diffusion zone. Figure 4(c) shows the kernel average misorientation map

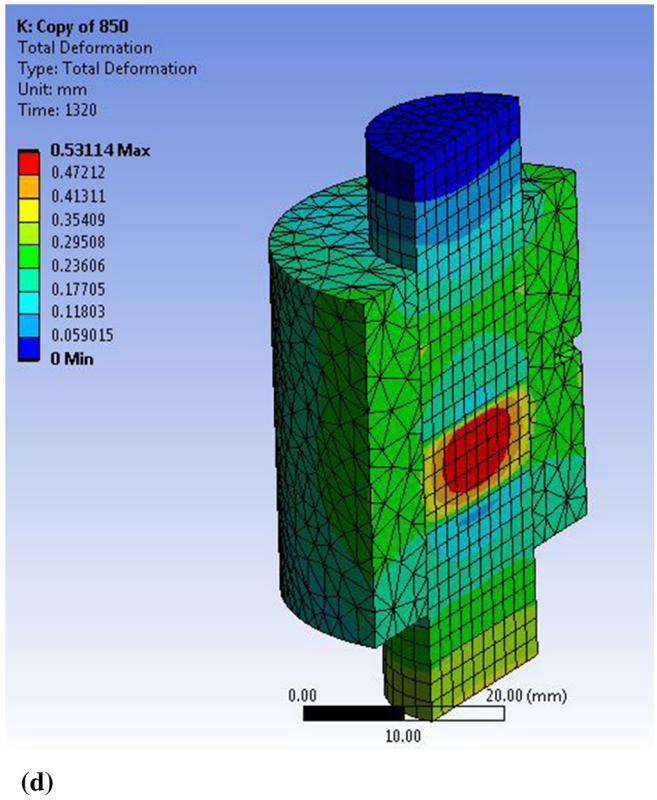
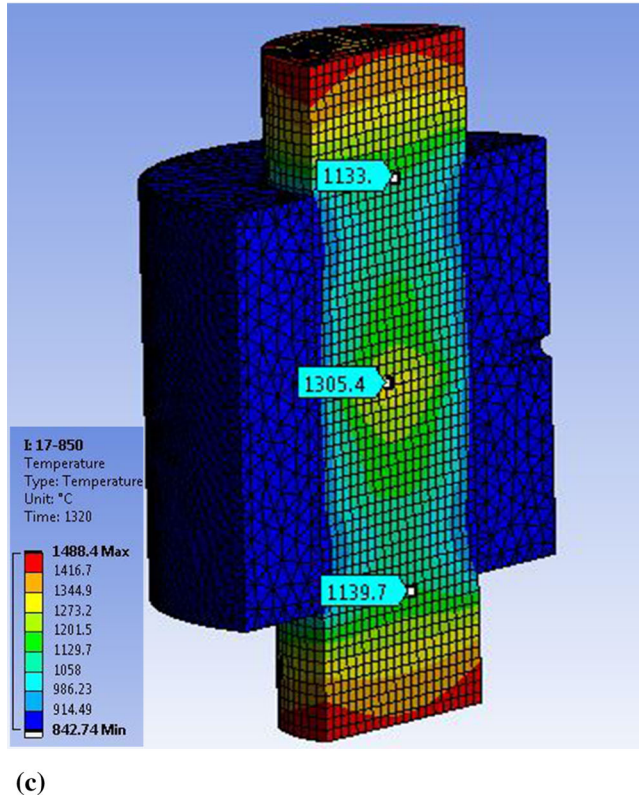
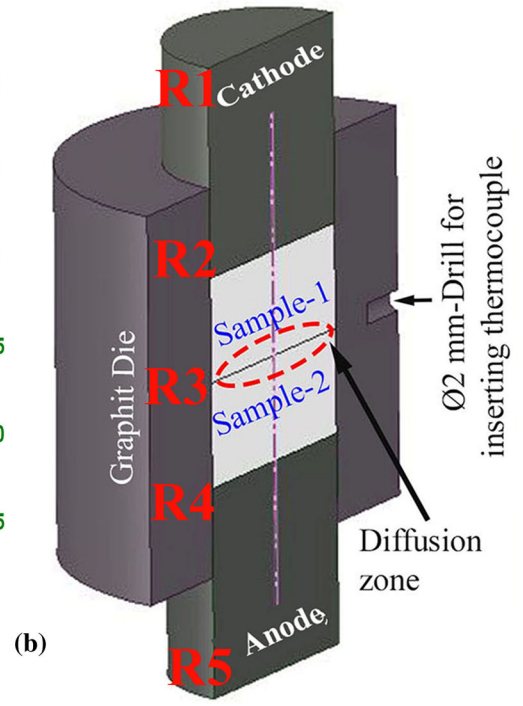
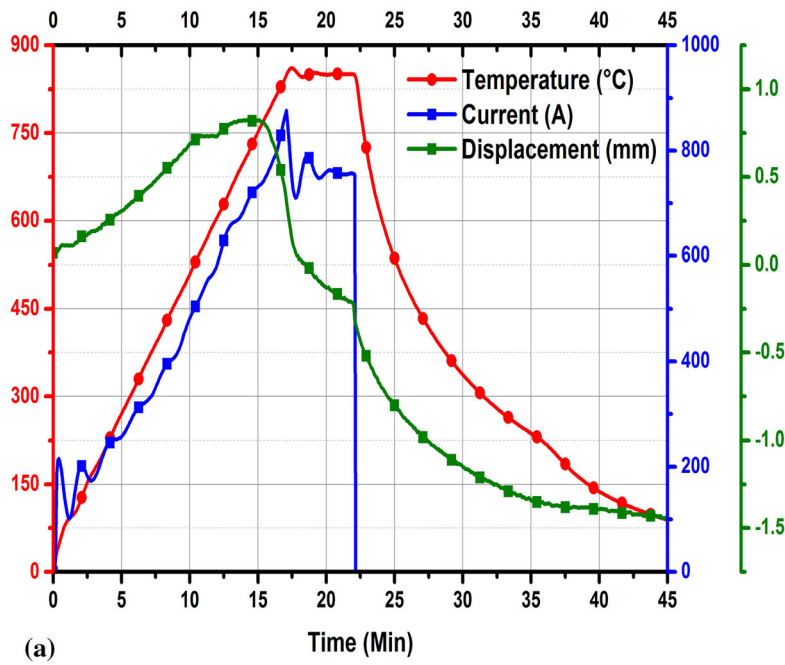


Fig. 2 (a) Time vs. temperature–current–displacement curves; Ansys simulation at 850 °C on (b) temperature distribution and (c) total deformation

(KAM) after SPS diffusion bonding at a pressure of 50 MPa. The diffusion zone is free from local residual plastic strain, and the 17-4 PH has appeared to have a minimum strain distribution compared to In 718.

Figure 5(a) and (b) shows the magnified image of IQ Map and OIM with IPF at the diffusion zone, which reveals randomly orientated elongated grains. Owing to the localized melting, the diffusivity of highly concentrated elements of Inconel 718 like Ni, Cr, Nb, Ti, and Al toward the 17-4PHSS

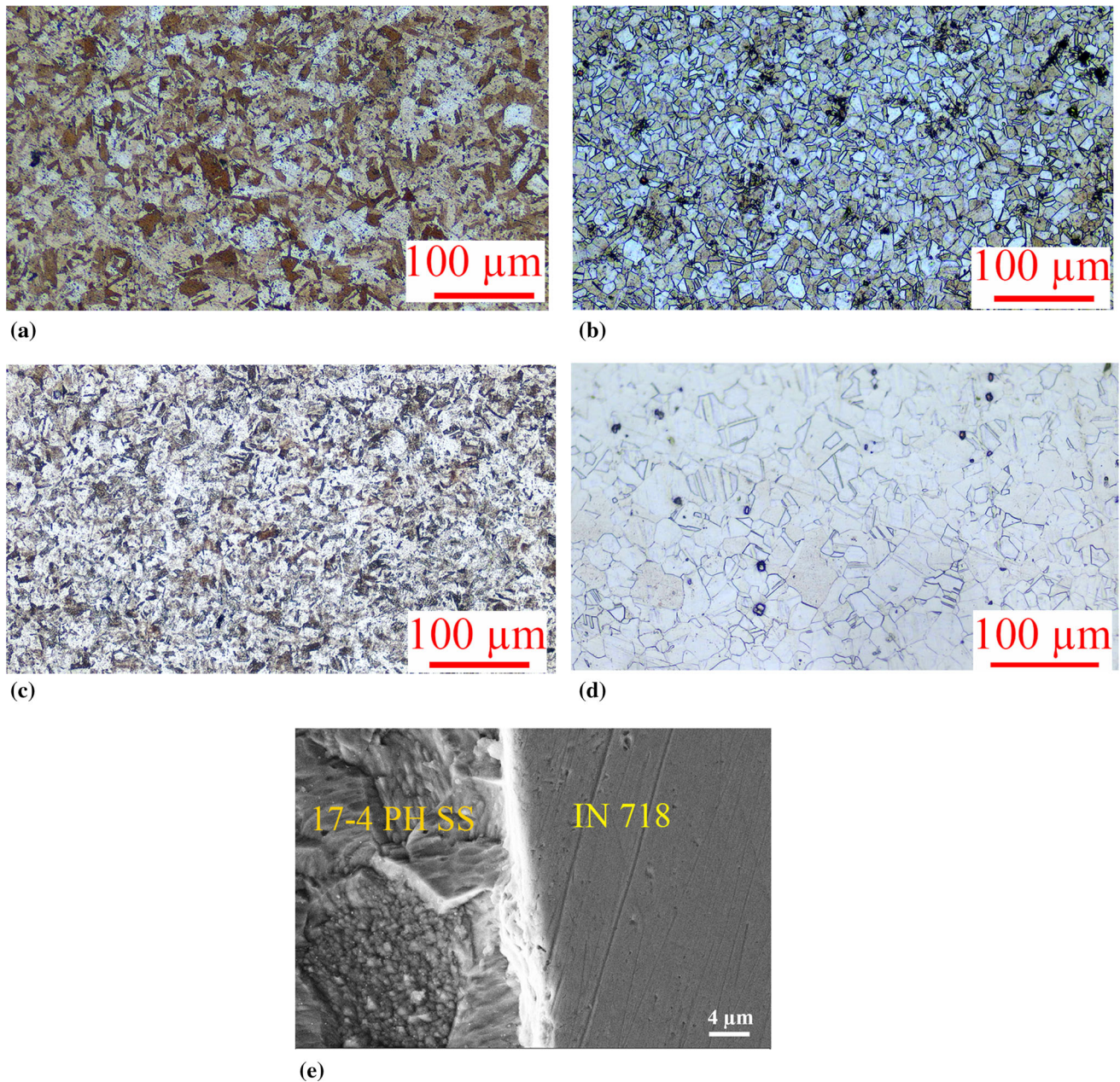


Fig. 3 Optical microstructure of 17-4 PH SS and IN 718: (a) and (b) as-received condition, (c and d) after diffusion bonding and (e) dissimilar joint

side and followed by a solidification effect. Figure 5(c) shows the phase map at the diffusion zone; there is an extent of the FCC phase (Inconel 718) up to $2 \mu\text{m}$ on the BCT phases (17-4 PH SS) side from the bond line, due to the diffusivity of austenite stabilizer of Ni. Figure 5(d) plots the results of the electron probe micro-analyzer (EPMA), The above-said elemental flow conditions are proved by the EPMA results. There is a diffusion of Ni, Cr, Nb, Ti, and Al from higher (IN 718) to lower concentration (17-4 PHSS) side up to $2 \mu\text{m}$.

3.4 Mechanical Properties and Fracture Analysis

Figure 6(a) shows the variation in hardness of as-received samples (black line) and SPS bonding (red line). The hardness values of Inconel 718 drop down from $541 \pm 5 \text{ Hv}$ (as-

received conditions) to $243 \pm 8 \text{ Hv}$ (after SPS diffusion bonding), and the same trend is noticed in 17-4PH SS with the average hardness of $342 \pm 10 \text{ Hv}$ and it is reduced to $297 \pm 5 \text{ Hv}$. After SPS diffusion bonding, the precipitates and carbides along grain boundaries get dissolved into the primary matrix, resulting in a reduction in hardness. At the diffusion zone, there is an increase in hardness of $345 \pm 10 \text{ Hv}$ due to the diffusion of Ni and other elements like Cr, Nb, Ti, and Al at a bonded zone.

Figure 6(b) shows the bar chart of engineering stress–strain for various processing conditions. In the as-received condition, yield strength and ultimate tensile strength of Inconel 718 are $1183 \pm 5 \text{ MPa}$, 1370 ± 10 and 17-4 PHSS are $785 \pm 5 \text{ MPa}$ & $1147 \pm 4 \text{ MPa}$, respectively. The SPS diffusion-bonded

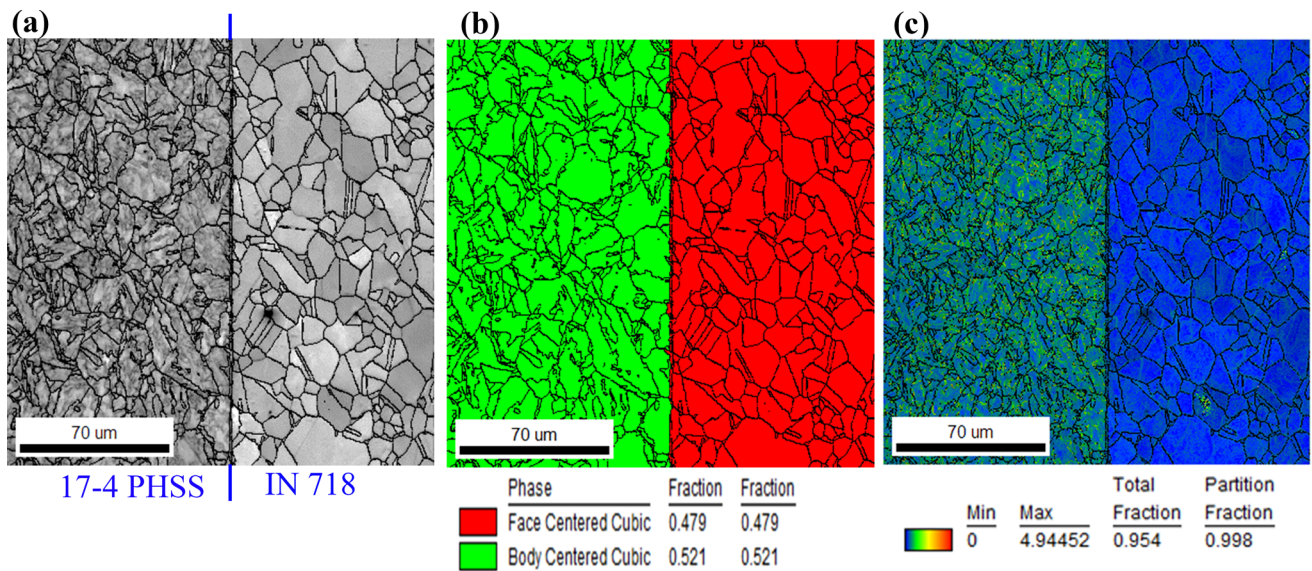


Fig. 4 EBSD studies on the bonded zone: (a) IQ map, (b) phase map, (c) OIM with IPF, and (d) KAM map

Table 3 Data derived from the Tafel plot

S.No	Condition	E_{corr} , mV	i_{corr} , $\mu\text{A}/\text{cm}^2$	Corrosion rate, mm/yr	R_p , K ohm cm^2
1	As-received IN 718	-310.988 ± 6	0.036 ± 0.05	4.44×10^{-4}	263
2	As-received 17-4 PH SS	-260.446 ± 4	0.168 ± 0.03	20.72×10^{-4}	105
3	SPS IN 718 Side	-302.498 ± 5	0.156 ± 0.04	20.99×10^{-4}	133
4	SPS 17-4 PH side	-358.953 ± 8	0.490 ± 0.05	65.93×10^{-4}	62
5	Diffusion zone	-217.273 ± 5	0.250 ± 0.03	32.20×10^{-4}	68

samples have yield strength of 429 ± 10 MPa and its ultimate strength is 708 ± 5 MPa with an elongation of $9 \pm 2\%$. The failure happened in the diffusion zone, particularly at the $2 \mu\text{m}$ thickness region.

Fractographical analysis with the elemental concentration and mapping is shown in Fig. 7. The strain-free brittle fracture is observed in Fig. 7(a); at point 1, there is an elemental concentration of both iron and nickel at equal proportions that are evolved. The agglomerated particles (Point 2) are distributed uniformly at the fracture surface. The particles magnified with their concentration are mentioned in Fig. 7(b), where Inconel 718 precipitate elements of niobium having a weight percentage of more than 75% followed by titanium at around 6% have been agglomerated at the bonded zone. The elemental mapping has been witnessed in the above statement with the segregation of niobium and titanium (particles in yellow color). There is even distribution of diffused elements like Ni, Cr, and Fe in the fracture surface, and the other elements Nb, Ti, and C are agglomerated and initiate the strain-free fracture.

3.5 Corrosion Behavior

Figure 8(a) shows the potentiodynamic polarization curves of IN 718, 17-4 PH stainless steel at as-received and SPS heat-affected zone followed by diffusion conduit zone using 3.5 wt.% of NaCl. The corresponding corrosion potential (E_{corr}), current density (i_{corr}), and polarization resistance (R_p) are listed in Table 3. The as-received IN 718 and 17-4PH have higher corrosion resistance when compared to spark plasma heat-affected IN718 and 17-4PHSS. IN 718 at high-temperature conditions, high-energy compounds like δ phases and Nb-rich M_{23}C_6 carbides present in the grain boundaries dissolve in the main matrix (Ref 22). The 17-4PHSS at the sensitizing temperature leads to fine grains with chromium depletion and forms intergranular corrosion (Ref 23). The diffusion zone consists of Nb and Ti-rich carbide forming elements that lead to corrosion up to 32.20×10^{-4} mm/yr.

Figure 8(b) shows the Nyquist plots; under varying conditions, the as-received Inconel 718 had lower film resistance (R_f), which guides to diffuse with the electrode surface and forms a passive layer that leads toward a higher-

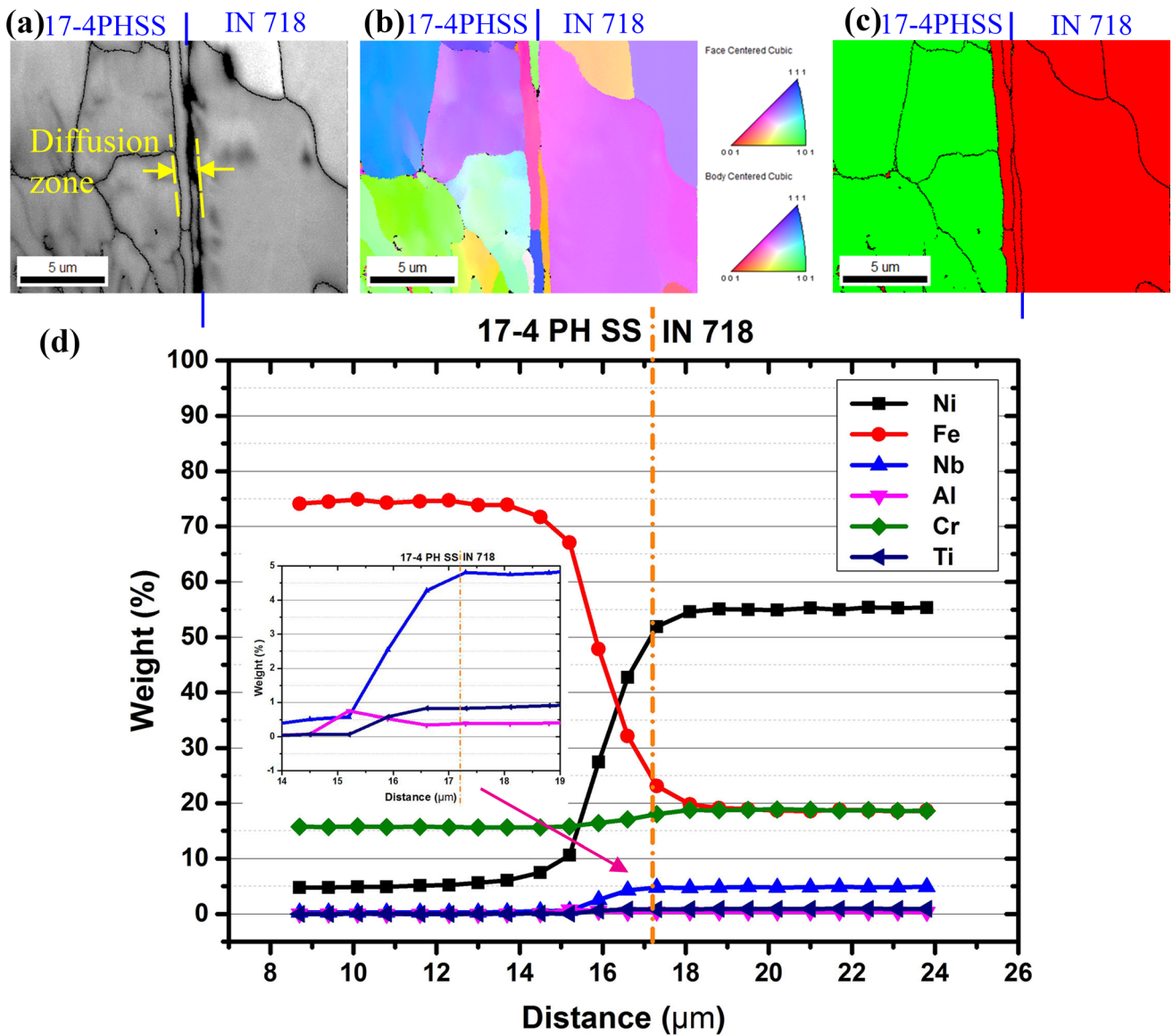


Fig. 5 EBSD studies on the bonded zone: (a) IQ map, (b) phase map, (c) OIM with IPF, (d) EPMA elemental distribution

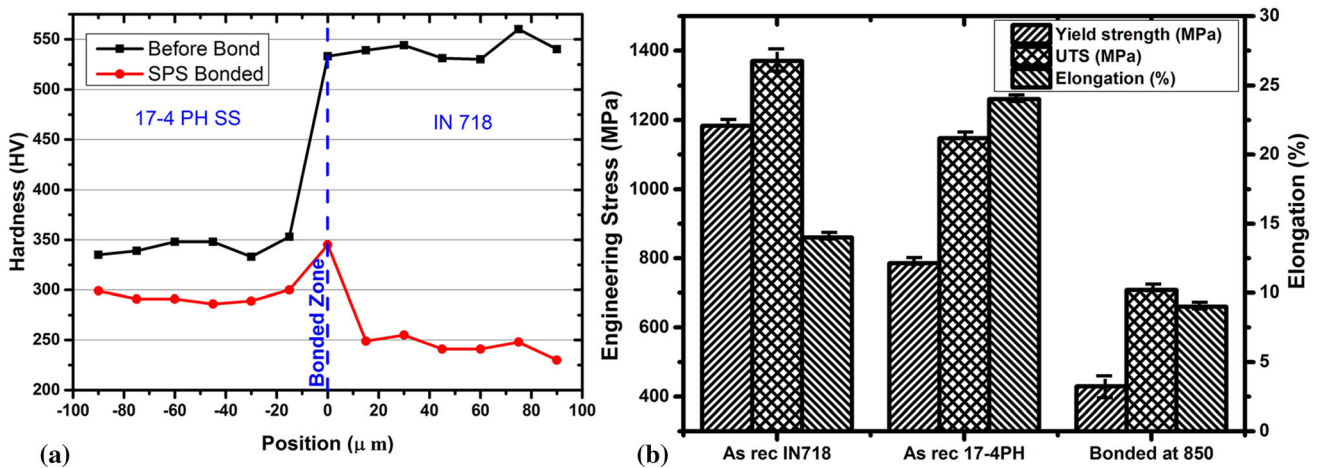


Fig. 6 (a) Vickers micro-hardness, (b) tensile data of as-received and diffusion-bonded samples (Color figure online)

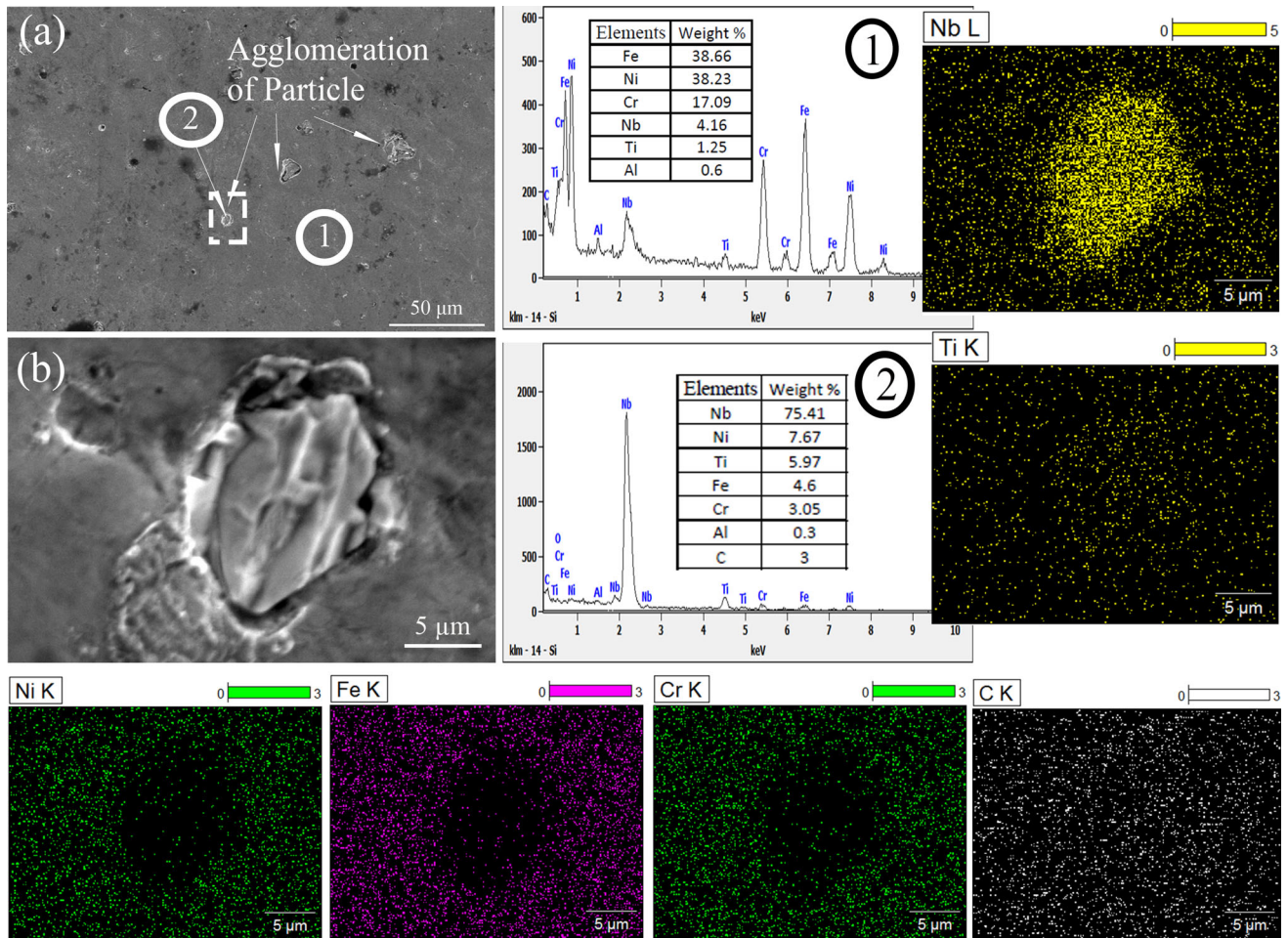


Fig. 7 Fractography with (a) elemental concentration and (b) elemental mapping on the fractured surface

frequency region, and the other samples gradually fall toward a lower-frequency region. There is a reduction in charge transfer resistance (R_{ct}) after SPS processing, and the lowest R_{ct} was recorded on the 17-4 PH side after SPS diffusion bonding. Figure 8(c) shows the equivalent circuit for fitting the Impedance data and their values are plotted in Table 4.

4. Conclusion

The dissimilar diffusion bonding was successfully obtained using the SPS heating technique. The diffusion

bonding was completed in a short duration of 5 min without any voids and nugget formation. Temperature distribution and total displacement were understood using Ansys simulation. There is a diffusion of Ni, Cr, Nb, Ti, and Al from higher (IN 718) to lower concentration (17-4 PHSS) side up to 2 μm . Niobium and Ti precipitates of Inconel 718 have been segregated at the bonded zone due to the resistance heating. Strain-free brittle fracture is due to the segregation of particles at the bonded zone. Dissolution of δ phases and Nb-rich $M_{23}C_6$ in Inconel 718 and fine grain with chromium depletion in 17-4PHSS leads to a higher corrosion rate after SPS diffusion bonding.

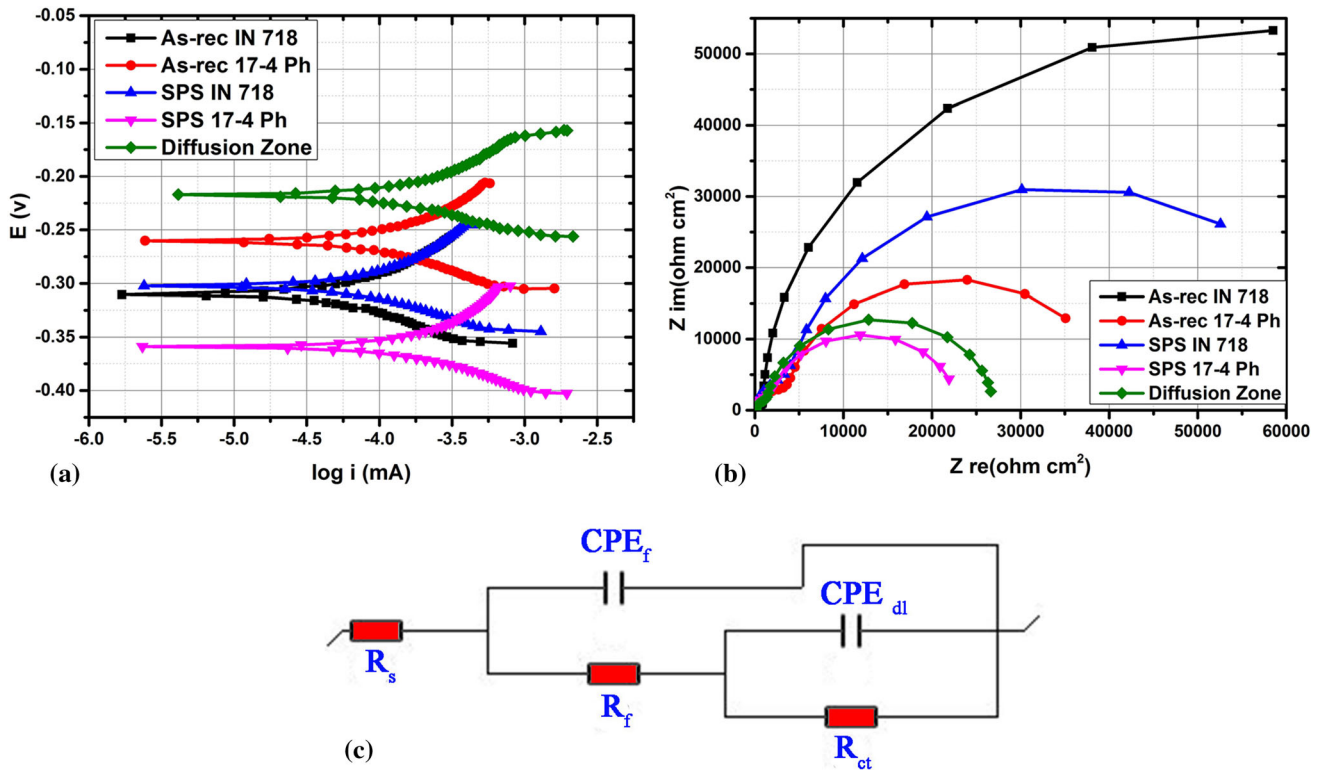


Fig. 8 (a) Potentiodynamic polarization curves, (b) Nyquist plots of as-received and diffusion-bonded samples and (c) equivalent circuit

Table 4 Data derived from the impedance curve

S. No.	Condition	$R_s, \Omega \text{ cm}^2$	$CPE_f \times 10^{-6}, F$	$R_f, \Omega \text{ cm}^2$	$CPE_{dl} \times 10^{-6}, F$	$R_{ct}, \Omega \text{ cm}^2$	$R_p, \Omega \text{ cm}^2$
1	As-received IN 718	23.03	18.02	1395	75.32	106,395	107,790
2	As-received 17-4 PH SS	41.88	30.93	5410	155.3	34,927	40,337
3	SPS IN 718 side	40.51	19.67	8476	46.64	58,054	66,530
4	SPS 17-4 PH side	34.78	16.31	3877	38.62	18,963	22,840
5	Diffusion zone	46.02	16.95	2461	50.83	24,404	26,865

References

1. T. Yokokawa, H. Harada, Y. Mori, K. Kawagishi, Y. Koizumi, T. Kobayashi, M. Yuyama, and S. Suzuki, Design of Next Generation Ni-Base Single Crystal Superalloys Containing Ir: Towards 1150 C Temperature Capability. In *Superalloys*, 2016, p 123–130
2. H. Zhang, R. Yan, B. Deng, J. Lin, M. Yang, and F. Peng, Investigation on Surface Integrity in Laser-Assisted Machining of Inconel 718 Based on In-Situ Observation, *Procedia CIRP*, 2022, **108**, p 129–134
3. N. Anbarasan, S. Jerome, and S.G.K. Manikandan, Hydrogen and Molybdenum Control on Laves Phase Formation and Tensile Properties of Inconel 718 GTA Welds, *Mater. Sci. Eng. A*, 2020, **773**, p 138874
4. S.G.K. Manikandan, D. Sivakumar, K.P. Rao, and M. Kamaraj, Effect of Weld Cooling Rate on Laves Phase Formation in Inconel 718 Fusion Zone, *J. Mater. Process. Technol.*, 2014, **214(2)**, p 358–364
5. S.G.K. Manikandan, D. Sivakumar, K.P. Rao, and M. Kamaraj, Effect of Enhanced Cooling on Microstructure Evolution of Alloy 718 Using the Gas Tungsten Arc Welding Process, *Weld. World*, 2016, **60(5)**, p 899–914
6. S.G.K. Manikandan, D. Sivakumar, K.P. Rao, and M. Kamaraj, Laves Phase in Alloy 718 Fusion Zone—Microscopic and Calorimetric Studies, *Mater. Charact.*, 2015, **100**, p 192–206
7. C. Zhong, A. Gasser, G. Backes, J. Fu, and J.H. Schleißenbaum, Laser Additive Manufacturing of Inconel 718 at Increased Deposition Rates, *Mater. Sci. Eng. A*, 2022, **844**, p 143196
8. D. Sidharth, R. Rajendran, and S. Narayanan, Microstructure and Properties of Inconel 718 and AISI 416 Laser Welded Joints, *J. Mater. Process. Technol.*, 2019, **266**, p 52–62
9. D. Bridges, C. Ma, S. Zhang, S. Xue, Z. Feng, and A. Hu, Diffusion and Wetting Behaviors of Ag Nanoparticle and Ag Nanowire Pastes for Laser Brazing of Inconel 718, *Weld. World*, 2018, **62(1)**, p 169–176
10. M.M.Z. Ahmed, B.P. Wynne, and J.P. Martin, Effect of Friction Stir Welding Speed on Mechanical Properties and Microstructure of Nickel Based Super Alloy Inconel 718, *Sci. Technol. Weld. Join.*, 2013, **18(8)**, p 680–687
11. H.R. Lashgari, S. Li, C. Kong, M. Asnavandi, and S. Zangeneh, Rotary Friction Welding of Additively Manufactured 17-4PH Stainless Steel, *J. Manuf. Process.*, 2021, **64**, p 1517–1528
12. Z. Guoge, R.S. Chandel, and H.P. Seow, Solid-State Diffusion Bonding of Inconel Alloy 718 to 17-4 PH Stainless Steel, *Mater. Manuf. Process.*, 2001, **16(2)**, p 265–279
13. P. Dong, Z. Wang, W. Wang, S. Chen, and J. Zhou, Understanding the Spark Plasma Sintering from the View of Materials Joining, *Scr. Mater.*, 2016, **123**, p 118–121
14. T. Nakamura, K. Hayakawa, S. Tanaka, H. Imaizumi, and Y. Nakagawa, Bonding Characteristics of Various Metals by DC Pulse Resistance Heat Pressure Welding, *Mater. Trans.*, 2005, **46(2)**, p 292–297
15. K. Zhao, Y. Liu, L. Huang, B. Liu, and Y. He, Diffusion Bonding of Ti-45Al-7Nb-0.3 W Alloy by Spark Plasma Sintering, *J. Mater. Process. Technol.*, 2016, **230**, p 272–279

16. P. Pripanapong, J. Umeda, H. Imai, M. Takahashi, and K. Kondoh, Bonding Mechanism of Ti/AZ80 Dissimilar Materials Fabricated by Spark Plasma Sintering, *J. Multidiscip. Eng. Sci. Stud.*, 2016, **2**(10), p 1009–1013
17. K. Ananthakumar and S. Kumaran, Experimental Investigation and Prediction of Optimum Process Parameter for Plasma Assisted Diffusion Bonding of Commercial Pure Titanium and Austenitic Stainless Steel, *Arab. J. Sci. Eng.*, 2019, **44**(2), p 1017–1032
18. O. Guillon, J. Gonzalez-Julian, B. Dargatz, T. Kessel, G. Schierming, J. Räthel, and M. Herrmann, Field-Assisted Sintering Technology/Spark Plasma Sintering: Mechanisms, Materials, and Technology Developments, *Adv. Eng. Mater.*, 2014, **16**(7), p 830–849
19. M. Radajewski, S. Decker, and L. Krüger, Direct Temperature Measurement via Thermocouples Within an SPS/FAST Graphite Tool, *Measurement*, 2019, **147**, p 106863
20. U. Anselmi-Tamburini, S. Gennari, J.E. Garay, and Z.A. Munir, Fundamental Investigations on the Spark Plasma Sintering/Synthesis Process: II. Modeling of Current and Temperature Distributions, *Mater. Sci. Eng. A*, 2005, **394**(1–2), p 139–148
21. Y. Mo, D.Z. Wang, B. Jiang, Y.Y. Li, H.D. Liu, C.G. Wang, and J.T. Wang, Influences of Grain Size on Electrochemical Corrosion Behaviors of Nickel-Based Alloy 718. In *Materials Science Forum* (Vol. 852, pp. 105–112). Trans Tech Publications Ltd. (2016)
22. R. Baldan, A.A.A.P.D. Silva, T.M. Tanno, E.T.D. Costa, J.V.N. Brentegani, and A.A. Couto, Experimental Investigation of Delta Phase Precipitation in Inconel 625 Superalloy Aged at 550, 625 and 725° C. *Mater. Res.*, 2020, **23**(1), e20190546
23. S.S.M. Tavares, F.J. Da Silva, C. Scandian, G.F. Da Silva, and H.F.G. De Abreu, Microstructure and Intergranular Corrosion Resistance of UNS S17400 (17-4PH) Stainless Steel, *Corros. Sci.*, 2010, **52**(11), p 3835–3839

Publisher's Note Springer Nature remains neutral with regard to jurisdictional claims in published maps and institutional affiliations.

Springer Nature or its licensor (e.g. a society or other partner) holds exclusive rights to this article under a publishing agreement with the author(s) or other rightsholder(s); author self-archiving of the accepted manuscript version of this article is solely governed by the terms of such publishing agreement and applicable law.